

CHAPTER 3

Melting temperature and catalytic activation energy of metallic nanoparticles

3.1 Introduction

Melting point depression was predicted in 1909 by Pawlow [1]. Takagi first observed melting point depression of several types of metal nanoparticles in 1954 and estimated the melting temperature from the electron beam energy and diffraction patterns [2]. Melting point depression is a very important parameter to be studied for applications involving nanoparticles, as it decreases the functional range of the solid phase. Nanoparticles are currently used or proposed for prominent roles in catalyst, sensor, medicinal, optical, magnetic, thermal, electronic, and alternative energy applications [3].

Many theoretical models were proposed for the study of melting temperature of the (assumed spherical) NPs. As melting initiates from surface, the surface to volume ratio for different shapes will vary from shape to shape. Therefore, shape becomes an important variable to be included in the study of melting temperature of the nanoparticles which was further experimentally demonstrated that the change in the shape shows depression in melting temperature [4].

A link between melting temperature and catalytic activation energy (CAE) has been discussed by Lu and Meng [5] and also investigated the impact of size and shape on CAE of the nanoparticle, thus, CAE becomes an important kinetic parameter to be studied in the field of nanocatalysis.

3.2 Influence of size, shape and dimension on melting temperature

In this section, we have investigated size, shape and dimension effect on melting temperature for free as well as embedded noble metallic nanoparticles. Noble metallic nanoparticles of silver, indium, lead is selected for different shapes and dimensions for size dependent melting

temperature. Our model is used for calculations and the results are further compared with other models and available results.

3.2.1 For freestanding nanoparticles

To calculate size, shape and dimension dependent melting temperature of metallic nanoparticle we have used the following equation of our model which is derived in chapter 2.

$$\frac{T_{mn}}{T_{mb}} = \left(1 - \frac{N}{2n}\right) \quad (3.1)$$

where T_{mn} , T_{mb} represents the melting temperature of nanoparticles and bulk respectively. $N/2n$ represents the shape with dimension. Following data from Table 3.1 is used for present calculations.

Table 3.1: Atomic diameter and melting temperature of the bulk element.

Element	Atomic diameter (h)	Melting temperature(T_{mb})
Ag	0.289	1235
Ni	0.249	1728
Pb	0.350	600.6
Al	0.286	933.47
In	0.325	430
Pt	0.278	2041
Zr	0.320	2128

Results of present model are compared with the outcomes by models of Nanda et al[6], Qi et al[7] and Bhatt et al[8]. As all the three models were formulated with the common ground of cohesive energy, hence we have selected them for comparative study.

Fig. 3.1(a) presents a comparison between the present work, theoretical models, experimental results[9] and molecular dynamics data[10] for free spherical Ag nanoparticles in terms of melting temperature as a function of size. It is observed from graph that melting temperature of Ag nanoparticles is found to decrease with decrease in size. Our model[11] is found more consistent with experimental and molecular simulation data as compared to other theoretical models in this case. Difference in the values of $N/2n$ for present model and Qi's model is clearly shown in Table 3.2.

Table 3.2: Comparison of $N/2n$ values between Present and Qi's model for various shapes.

Shapes of particles	Present model [11]	Qi's model [7]
Spherical/Cubical	3h/D	2h/D
Tetrahedral	7.35 h/D	4.89h/D
Octahedral	3.69h/D	2.44h/D
Icosahedral	1.98h/D	1.32h/D
Cylindrical Wire	2h/D	1.33h/D
Thin Film	h/D	0.66h/D

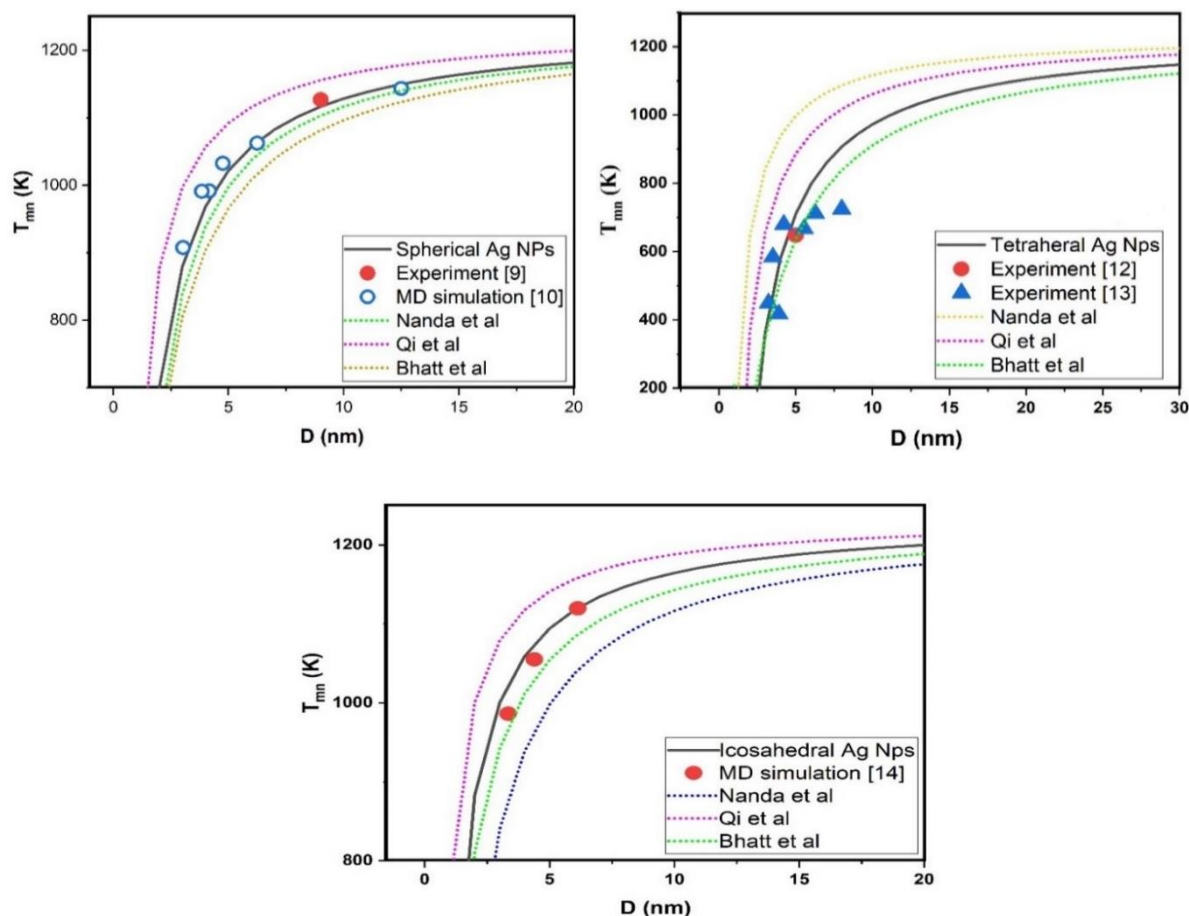


Figure 3.1: Size dependent melting temperature of (a) spherical Ag NPs (b) tetrahedral Ag NPs (c) icosahedral Ag NPs.

Fig. 3.1(b) and (c) shows melting temperature of tetrahedral and icosahedral Ag nanoparticles as function of size. The results obtained from Equation 3.1 are further compared with selected theoretical models. In both the graphs our calculated results are found more consistent with experimental [12,13] and molecular stimulation data[14] rather than other models. It is observed that our predictions are found intermediate between Qi's model[7] and Bhatt's model[8] for tetrahedral and icosahedral Ag nanoparticles. While Nanda's model[6] showed consistent results with our model for spherical Ag NPs. A rapid drop in melting temperature is seen for size below 10 nm in case of Ag NPs. Thus by comparing Fig. 3.1(a), (b) and (c) we found the sequence of melting temperature as $T_m(\text{tetrahedral}) < T_m(\text{spherical}) < T_m(\text{icosahedral})$ for constant size.

Fig. 3.2(a) shows melting temperature of spherical indium nanoparticles as a function of size. Our model is found more consistent with experimental data [15] and [16] as compared to [17] where Nanda's model[6] shows good reliability with experimental data[17]. It can be seen from that Bhatt's model overlaps our values of $T_{mn} < 280$ K and thereafter it diversifies for higher temperatures. Moreover, on comparing the results of all the three models with present model, our results are found more fruitful. Experimentally, it is observed that melting temperature of a particle with a fixed radius depends on rate of melting and surface area which in turn affects the heating rate. $T_{mn}(D)$ value at a low heating rate is always smaller than that at a high heating rate which in turn becomes the reason for low melting of nanoparticles for experimental data[17].

Further to affirm our model for dimension $d=1$ in case of In nanowire, Fig. 3.2(b) shows the melting temperature as a function of size. A good accordance is observed for In nanowire with $D < 7$ nm with both the experimental values[18,19]. But deviations in calculated values and experimental values are found for size $D > 7$ nm. We also observed that Qi's model[7] showed highest melting temperature while Nanda's model[6] showed least melting temperature for constant sized In nanowire among all the four models.

Fig. 3.2(c) shows a comparison of In nanofilm with dimension $d=2$ with size for T_{mn} . T_{mn} is found to decrease with decrease in size for all models. Present model is found consistent with the available experimental data[20]. In Fig. 3.2 it is observed that our calculated values are found intermediate between Qi's model and Nanda's model, here Bhatt's model is not considered because the values will vary according to the selection of k 's value.

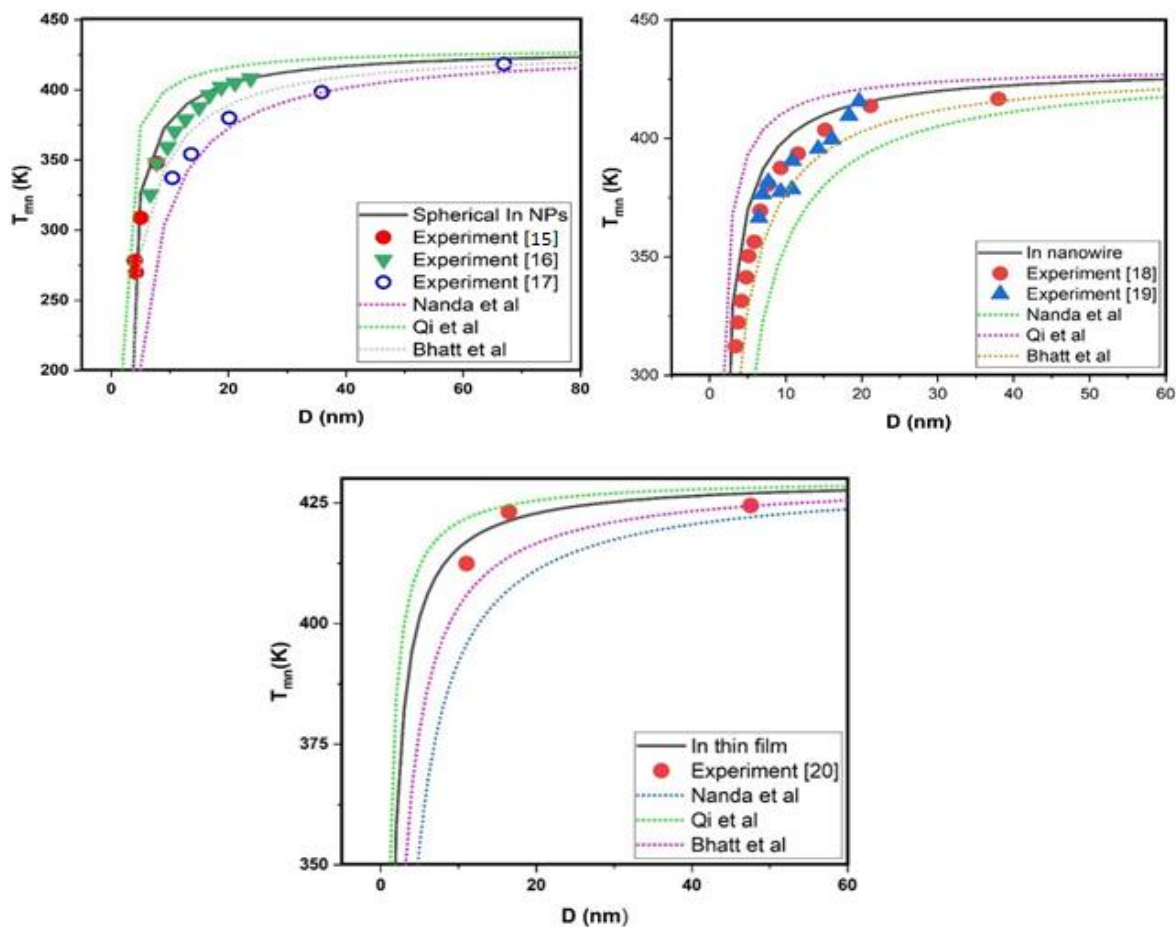


Figure 3.2: Size dependent melting temperature of (a) spherical In NPs (b) In nanowire (c) In thin film.

Fig. 3.3 shows the size and dimensional effects on the melting temperature of freestanding Lead (Pb) nanoparticles. It is found from Fig. 3.3(a) that T_{mn} of spherical Pb nanoparticles decreases with decreasing size and the drop becomes dramatic when D is below 10 nm. Present model is compared with the available experimental data [15,17] and molecular dynamics (MD) simulations data [21] in order to check its validity in case of Pb nanoparticles. A good accordance is observed between the calculated values, MD simulations [21] and experimental data [15]. However, in case of Pb cylindrical nanowire, sharp decrease in T_{mn} occurs for $D < 7$ nm as seen in Fig. 3.3(b). It is also observed that MD simulation data [21] is intermediate between Present model and Qi's model in case of Fig. 3.3(b). Comparison between T_{mn} of free Pb nanoparticles as a function of size with respect to different dimensions is shown in Fig. 3.3(c),

where Pb nanoparticles with dimension $d=0$ and $d=2$ shows least and highest melting temperature at constant size respectively.

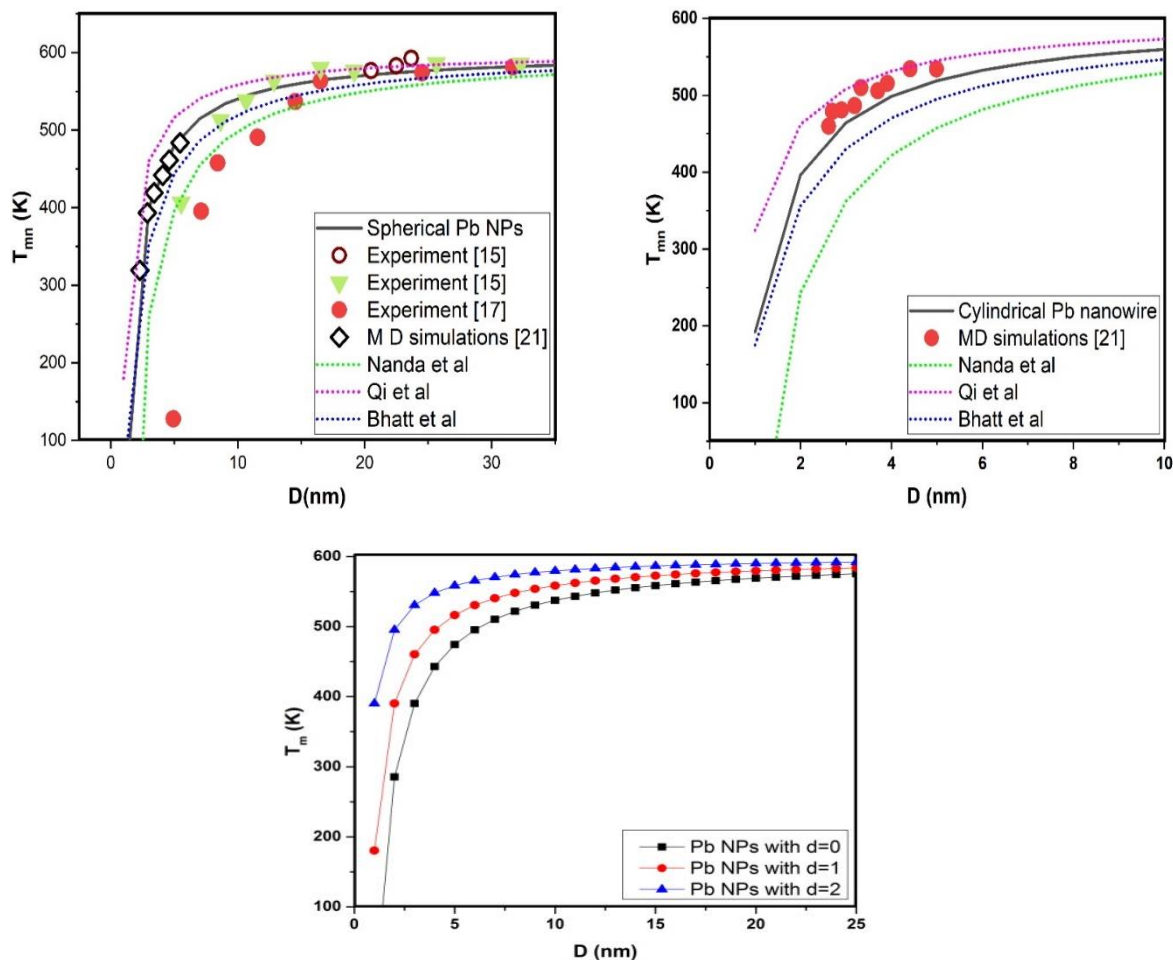


Figure 3.3: Size dependent melting temperature of (a) spherical Pb NPs (b) cylindrical Pb nanowire (c) Pb NPs with different dimensions.

Moreover to find the surface to volume ratio for different dimensions and to compare them, we have used $N/2n$ values of our model from chapter 2. Thus by taking the ratio of

$N/2n (d=2)/ N/2n (d=0) : N/2n (d=1)/ N/2n (d=0) : N/2n (d=0)/ N/2n (d=0)$ for constant size, we get $(h/D) / (3h/D) : (2h/D) / (3h/D) : (3h/D) / (3h/D)$ and the ratio turns out to be as 1 : 2 :

3. We also calculated $\frac{T_{mb}-T_{mn}}{T_{mb}}(spherical) : \frac{T_{mb}-T_{mn}}{T_{mb}}(wire) : \frac{T_{mb}-T_{mn}}{T_{mb}}(film)$ using our model for constant size and we get the ratio as (sphere:wire:film) = (3:2:1) which is exactly seen in Nanda's work[18] which implies that their rate of decrease of the melting temperature

for different low-dimensional systems, is in accordance with the predicted behavior from thermodynamical considerations[22].

From all the above cases, it is observed that melting temperature decreases with decrease in size at nanoscale and with increase in shape factor. As the scale increases melting temperature gradually reaches towards bulk melting point and all the dimensions seems to merge with each other with $D > 50\text{nm}$.

3.2.2 For nanoparticles embedded in a matrix

It becomes very important to study about the behavior of embedded nanoparticles because of its recent applications[23-26] which is discussed in chapter 1 in detail. One important phenomena known as superheating was discovered during the study of embedded nanoparticles in some matrix. We have used the below given equation from chapter 2 of our model for calculating the size, shape, dimension and matrix dependent melting temperature of Ag/Ni, In/Al and Pb/Al.

$$\frac{T_{mn}}{T_{mb}} = \left[1 - \frac{N}{2n} \left(1 - \frac{T_M}{T_{mb}} \right) \right] \quad (3.2)$$

Fig. 3.4 compares the melting temperature T_{mn} of embedded Ag nanoparticles in Ni matrix (Ag/Ni) as a function of size D for (a)icosahedral (b)different shapes and (c) different dimensions using Equation 3.2 of present model and further compared with available experimental data[27] and other models[6,7,8]. From Figure 3.4 it is observed that melting temperature is found to decrease with increase in size irrespective of shape and dimension in all the cases.

Fig. 3.4(a) shows superheating of embedded Ag nanoparticles which is just the reciprocal behavior of free Ag nanoparticles. Moreover as the size increases beyond 50 nm, T_{mn} will tend to reach the bulk melting temperature irrespective of different shapes and dimensions. A good consistency is observed for embedded icosahedral Ag/Ni nanoparticles between the calculated values and experimental data[27]. Intimacy between present model and Qi's model is observed. Fig. 3.4(b) shows the tendency of depression in T_{mn} as a function of size which follows the sequence: T_{mn} (tetrahedral) > T_{mn} (octahedral) > T_{mn} (spherical or cubical) > T_{mn} (icosahedral) for embedded Ag nanoparticles with $d=0$ at constant nanosize. Moreover in terms of dimensions, T_{mn} follows the sequence as T_{mn} (sphere/ 0-d) > T_{mn} (wire/1-d) > T_{mn} (film/2-d) with constant nanosize for embedded Ag nanoparticles as shown in Fig. 3.4(c).

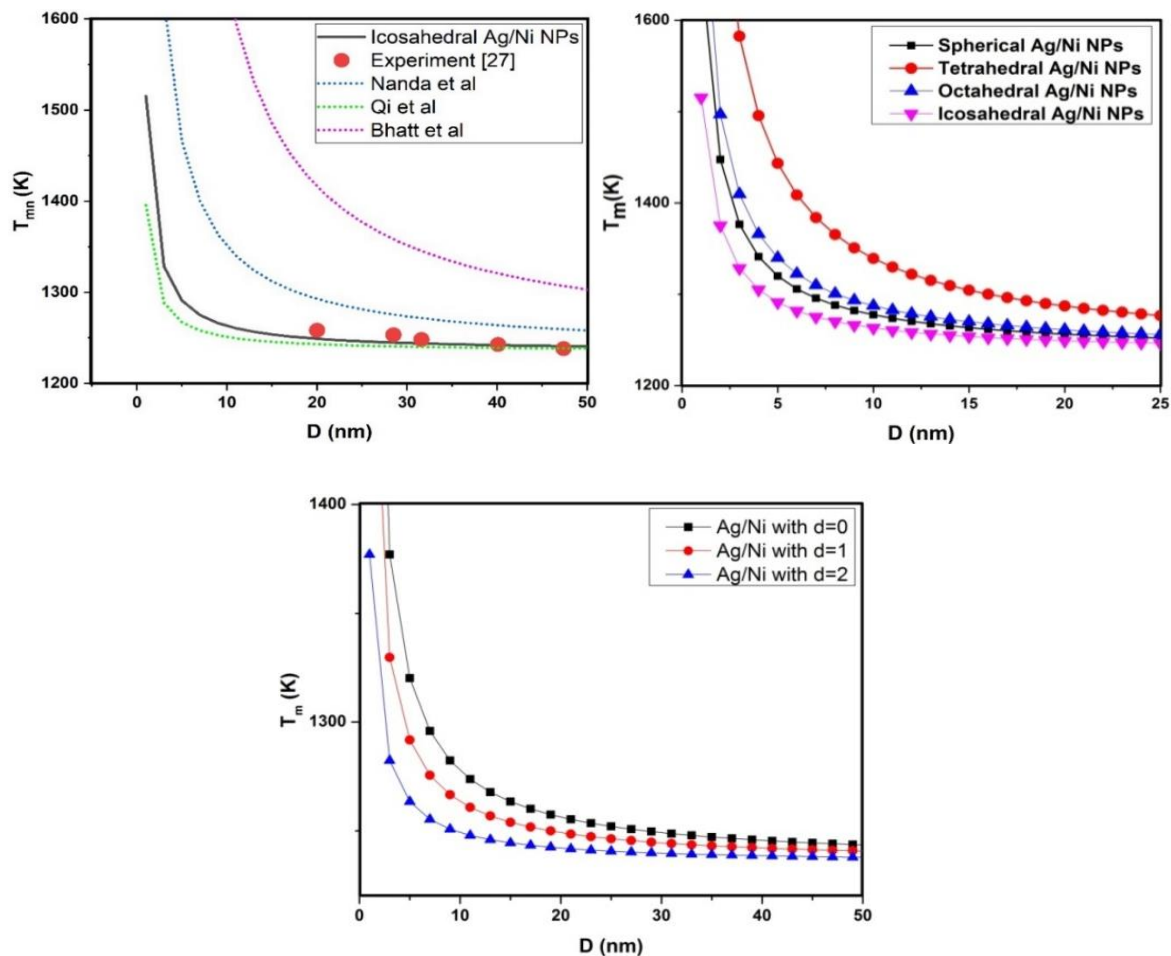


Figure 3.4: Size dependent melting temperature of embedded Ag nanoparticles in Ni matrix for (a) icosahedral (b) different shapes (c) different dimensions.

Comparisons between the model predictions by using Equation 3.2 and the available experimental results for superheating of spherical In/Al nanoparticles are shown in Fig. 3.5(a). Some differences exist between the predicted values and experimental results[28] for $D > 20$ nm. This may be due to the fact that the present model only considers the size effect, neglecting others such as, phonon softening at the surface, grain boundaries, disorder, defects, and impurities, which lead to the deviation from the experimental results. Also it is observed that experimental data of In/Al is lying in the proximity of our model and Qi's model[7]. However, it is possible that the shapes of nanoparticles at their corresponding experimental conditions could not be completely considered.

In Fig. 3.5(b) and 3.5(c) it is observed that melting temperature of embedded In NPs increases with decreasing size in case of different dimensions and different shapes respectively.

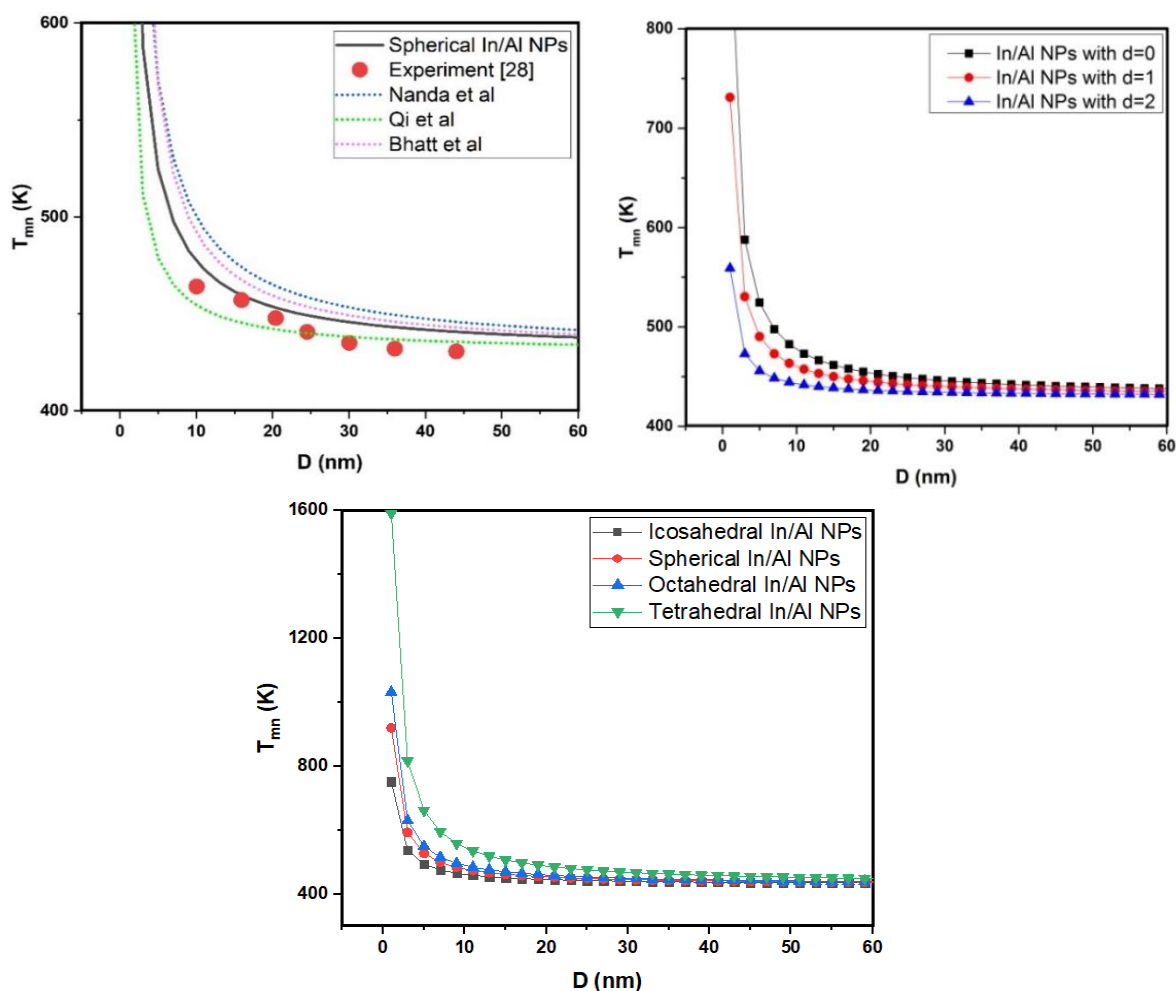


Figure 3.5: Size dependent melting temperature of In nanoparticles embedded in Al matrix for (a) spherical (b) different dimensions (c) different shapes.

Superheating is observed for Pb nanoparticles embedded in Al matrix as a function of size in Fig. 3.6. Moreover Fig. 3.6(a) shows a comparison of present model with different models and experimental results [29,30,31]. Nanda's model [6] is found consistent with experimental results of Graback and Bohr [31], however, work of Sheng [30] is in good accordance with present model. Here none of the model follows the experimental results of Chattopadhyay and Goswami [29] accurately. It is observed that Qi's model [7] underestimates the superheating of Pb nanoparticles. In Bhatt's model [8] by varying the negative value of k , the calculated values

can vary accordingly with the available experimental data[31]. Fig. 3.6(b) and 3.6(c) represents the T_{mn} of Pb/Al for different shapes and dimensions respectively as a function of size. Also it is seen that effect of shapes and dimensions diminishes for $D > 25$ nm.

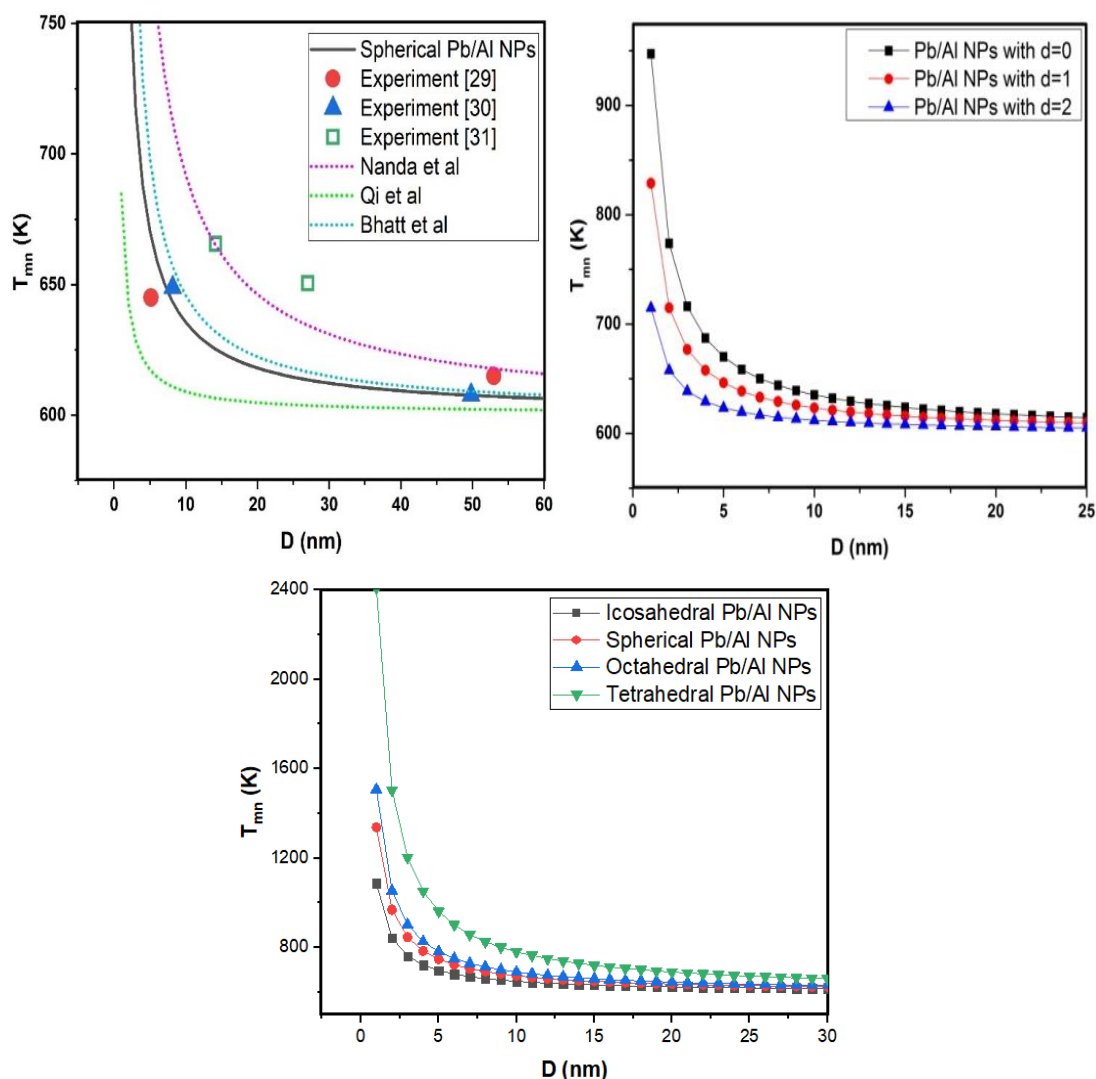


Figure 3.6: Size dependent melting temperature of Pb nanoparticles embedded in Al matrix for (a) spherical (b) different dimensions (c) different shapes.

From the above graphs and tables, T_{mn} is found different for various shapes/dimensions with constant nanosize. It can be very well understood with the fact that the shape determines the number of surface atoms which in turn decides the coordination number, bond strength and thus affecting melting temperature. In present model the shape is expressed by $\frac{N}{n}$ i.e. surface

to volume ratio of atoms for various shapes. According to Table 3.2 we interpret the sequence of $\frac{N}{n}$ as $\frac{N}{n}(\text{tetrahedral}) > \frac{N}{n}(\text{octahedral}) > \frac{N}{n}(\text{cubic/ sphere}) > \frac{N}{n}(\text{wire}) > \frac{N}{n}(\text{icosahedral}) > \frac{N}{n}(\text{film})$. The predicted values of the present model are found more consistent than all the three models, which in turn proves that the adopted method for the formulation of the model is appropriate. It is also observed that series of melting temperature T_{mn} (Qi's model) $> T_{mn}$ (present model) for constant size because $\frac{N}{n}(\text{Qi's model}) < \frac{N}{n}(\text{present model})$ and in turn deviates from the available experimental and MD simulation data. In all the three cases of embedded nanoparticles superheating is observed due to two reasons i) melting temperature of matrix is higher than the bulk embedded nanoparticle ii) coherent or semicoherent interface. Due to superheating the melting temperature of embedded nanoparticle showed inversely proportion to size but also claimed its variation due to shape and dimension at nanoscale.

3.3 Size, shape and dimension dependent catalytic activation energy

A link between melting temperature and catalytic activation energy (CAE) has been discussed by Lu and Meng [5] and also investigated the impact of size and shape on CAE of the nanoparticle. In the field of nanocatalysis, CAE becomes an important kinetic parameter to be studied. In this contribution, Narayanan and El-Sayed performed experiments to study the stability and CAE of tetrahedral, spherical and cubic platinum nanoparticles of 4.8 nm, 4.9 nm and 7.1 nm diameter for electron-transfer reaction between hexacyanoferrate (III) ions and thiosulphate ions [32,33]. It was found that the surface atoms present on the corners and the edges of tetrahedral platinum nanoparticles with (111) facets were more catalytically active than the surface atoms present on the corners and the edges of cubic nanoparticles with (100) facets. The catalytic activity of spherical nanoparticles was found to be intermediate between tetrahedral and cubic nanoparticles. Conclusion of the experiment was that the CAE of tetrahedral platinum nanoparticles was least and the CAE of cubic platinum nanoparticle was highest among the three shapes [32,33]. As a result, nanoparticles with well controlled size and shape of appropriate surface areas and crystallographic facets can be used for both selectivity and reactivity for many fruitful catalytic reactions ending in tremendous growth of nanocatalysis [32,34].

3.3.1 For freestanding nanoparticles

We have investigated the CAE of platinum nanoparticles by using below equation derived in chapter 2. A simple comparison of different shapes and different dimensions at constant size is done further.

$$\frac{E_{an}}{E_{ab}} = \left(1 - \frac{N}{2n}\right) \quad (3.3)$$

where E_{an} , E_{ab} represents the catalytic activation energy of nanoparticles and bulk respectively.

Variation in the ratio of Catalytic activation energy of the freestanding Platinum(Pt) nanoparticle and the bulk Pt of different shapes with respect to size of the nanoparticle can be observed clearly in Fig. 3.7(a). Least E_{an}/E_{ab} is observed for tetrahedral shaped Pt nanoparticles while highest E_{an}/E_{ab} is seen for icosahedral shaped Pt nanoparticles among the selected shapes for constant size. So we can predict that tetrahedral shaped nanoparticle can activate the catalytic process with least energy. Moreover, we can say that E_{an}/E_{ab} (tetrahedral) < E_{an}/E_{ab} (octahedral) < E_{an}/E_{ab} (spherical) < E_{an}/E_{ab} (icosahedral) with selected size D (nm).

In case of Fig. 3.7(b) it is observed that E_{an}/E_{ab} ($d=0$) < E_{an}/E_{ab} ($d=1$) < E_{an}/E_{ab} ($d=2$) for constant size. This sequence is observed because of $(3h)$ for $d=0$, $(2h)$ for $d=1$ and (h) for $d=2$ where h is atomic diameter. Prominent decrease in the ratio of catalytic activation energy is observed for the values of $D < 10$ nm only. Further increment in the size, the close proximity is observed for all the dimensions.

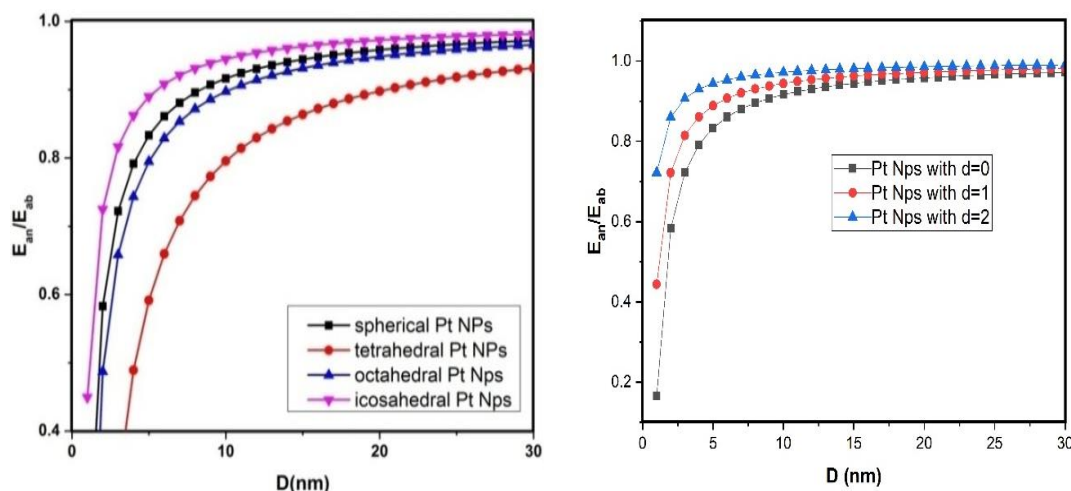


Figure 3.7 Size dependent ratio of catalytic activation energies of free Pt NPs for (a) different shapes and (b) different dimensions.

3.3.2 For nanoparticles embedded in a matrix

In this part, we have investigated the effect of matrix on the embedded platinum nanoparticle in terms of size, shape, dimension and matrix for catalytic activation energy. For the calculations we have used the equation of chapter 2.

$$\frac{E_{an}}{E_{ab}} = \left[1 - \frac{N}{2n} \left(1 - \frac{T_M}{T_{mb}} \right) \right] \quad (3.4)$$

The equation uses the terms of melting temperature of matrix and bulk melting temperature of embedded nanoparticle. Here the matrix used is zirconia whose melting temperature is higher than platinum. Fig. 3.8 represents the supercatalytic activation energy of embedded Pt nanoparticles in Zr matrix for various shapes as a function of size. As the melting temperature of Zr is greater than Pt and the interface between Pt and Zr is taken coherent so superheating is observed. The ratio of the catalytic activation energy of nanoparticle of selected size to the bulk is found increasing with decreasing size. This behaviour of embedded nanoparticle will be prominently seen for $D(\text{nm}) < 10$. But as the size increases beyond 100 nm,

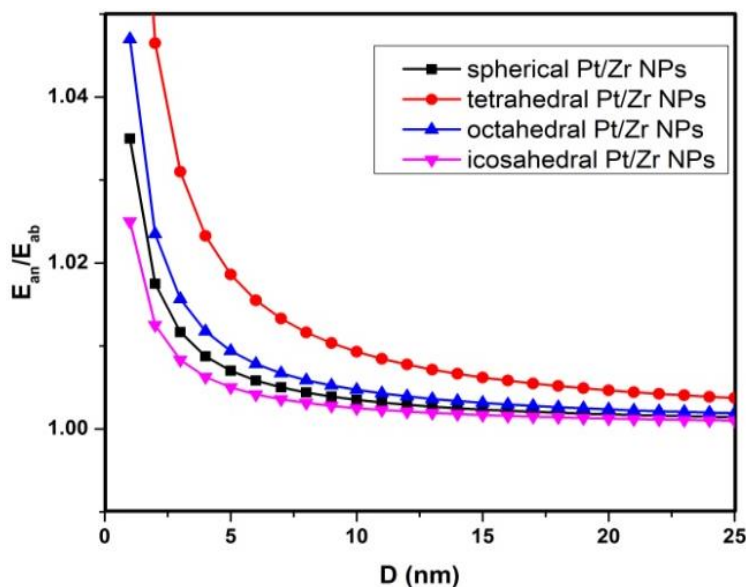


Figure 3.8: Size and shape dependent ratio of catalytic activation energies of embedded Pt NPs in Zr. ratio of catalytic activation energy becomes almost constant irrespective of the shapes. As observed from Fig. 3.8, tetrahedral and icosahedral shaped Pt embedded nanoparticle shows highest and lowest supercatalytic activation energy respectively.

3.4 Comparison of catalytic activation energy with different models

In order to investigate the catalytic properties of free and embedded nanoparticles and the role of surface for their effective activation energy we are using equation Equations 3.3 and 3.4 respectively. We have analyzed quantitatively the catalytic activity, by comparing the value of the catalytic activation energy of different shaped nanoparticles, catalyzing the same chemical reaction. In Fig. 3.9, the theoretical catalytic activation energies calculated from Equation 3.3 have been compared successfully with experimental data of platinum nanoparticles[32] and three models. Our calculated values are found more consistent in both the cases rather than Qi[7], Bhatt[8] and Guisbier model[35].

According to our model predictions, the ratio of the catalytic activation energies between tetrahedral ($D = 4.8$ nm) and spherical ($D = 4.9$ nm) pure platinum nanoparticle has been obtained 0.69 which shows good agreement with the experimental value of 0.62 ± 0.06 [32,36] and shown in Fig. 3.9. Further, calculating the ratio of the catalytic activation energies between cubic ($D = 7.1$ nm) and spherical ($D = 4.9$ nm) of pure platinum

nanoparticle and determined as 1.06 which shows excellent agreement with the experimental value of 1.17 ± 0.12 [32,36] and shown in Fig. 3.9.

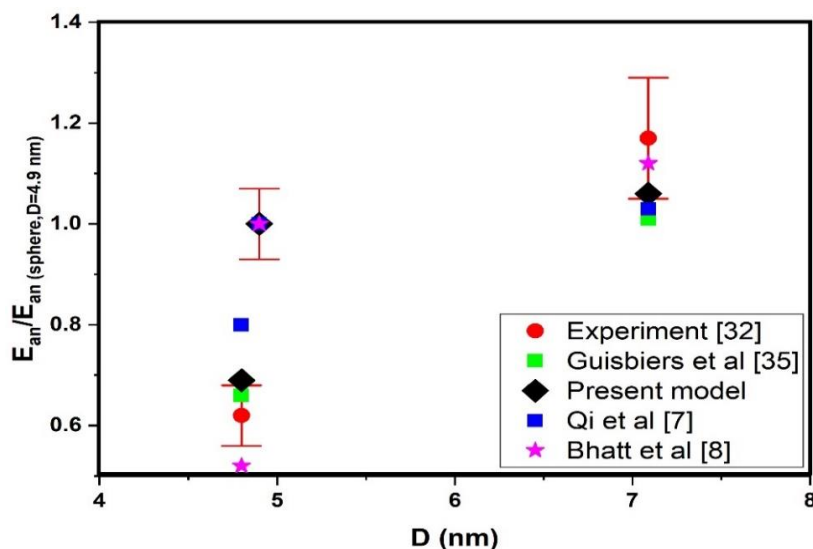


Figure 3.9: Size-dependent catalytic activation energy of Platinum for sphere, cube and tetrahedron nanoparticles with different models and experimental results.

3.5 Conclusions

In this chapter, we have investigated size, shape and dimension effect on melting temperature and catalytic activation energy of free as well as embedded nanoparticles. The validity of the model has been checked in terms of available experimental data, MD simulations and other model results. In case of freestanding nanoparticles, melting temperature and catalytic activation energy are found to decrease with decrease in size due to increase in N/n ratio. As a result, the sequence for melting temperature and catalytic activation energy for different shapes

follows: $[T_{mn}, E_{an}(\text{tetrahedral})] < [T_{mn}, E_{an}(\text{octahedral})] < [T_{mn}, E_{an}(\text{spherical})] < [T_{mn}, E_{an}(\text{icosahedral})]$ with selected size $D(\text{nm})$. Superheating was observed for embedded nanoparticles with a reason that the bond energy between the surface atoms of nanoparticles and the matrix atoms, is more strong than the bond energy between the interior atoms of nanoparticles and is possible with coherent or semi-coherent interface. As a result, the order of melting temperature and catalytic activation energy for embedded nanoparticle are found as, $[T_{mn}, E_{an}(\text{tetrahedral})] > [T_{mn}, E_{an}(\text{octahedral})] > [T_{mn}, E_{an}(\text{spherical})] > [T_{mn}, E_{an}(\text{icosahedral})]$

(icosahedral)] for selected size D(nm) which is just the reverse of the free standing nature of the nanoparticles. In our study we observed that the size plays primary role while shape and dimension plays secondary role for both the selected thermodynamical quantities within nanoscale limit. Moreover, the present model predictions are found very consistent for melting temperature and catalytic activation energy for the selected nanoparticles and hence can be employed to estimate the melting temperature and catalytic activation energy of any metallic nanoparticles with different morphologies in free as well as embedded form and becomes fruitful tool in the research of size, shape and dimension dependent properties of nanomaterial.

References

1. P. Pawlow, *Z. Phys. Chemie.* **65**(1), 545 (1909).
2. M. Takagi, *J. Phys. Soc. Jpn.* **9** (3), 359 (1954).
3. G. G. Wildgoose, C. E. Banks and R. G. Compton, *Small.* **2** (2), 182–93 (2005).
4. R. Goswami, K. Chattopadhyay, *Philos. Mag. Lett.* **68**, 215 (1993).
5. H. M. Lu and X. K. Meng, *J. Phys. Chem. C.* **114**, 1534–1538 (2010).
6. K.K. Nanda, S.N. Sahu, S.N. Behera, *Phys. Rev. A.* **66**, 13208 (2002).
7. W.H. Qi, M.P. Wang, *Materials Chemistry and Physics.* **88**, 280–284 (2004).
8. S. Bhatt, M. Kumar, *Journal of Physical and Chemistry of Solids.* **106**, 112-117 (2017).
9. S. C Tang, S. P Zhu, H. M. Lu, X. K. J. Meng, *Solid State Chem.* **181**, 587 (2008).
10. S. F. Xiao, W. Y. Hu, J. Y. Yang, *J. Phys. Chem. B.* **109**, 20339 (2005).
11. C. S. Tiwari, A. Pratap and P.K. Jha, *J Nanopart Res.* **22**, 218 (2020).
12. M. A Gracia-Pinilla, E. Perez-Tijerina, J. A. Garcia, *J.Phys. Chem. C.* **112**, 13492 (2008).
13. T. Castro, R. Reifenberger, E. Choi, R. P. Andres, *Phys. Rev. B.* **42**, 8548 (1990).
14. S. J. Zhao, S. Q. Wang, D. Y. Cheng, H. Q. Ye, *J. Phys. Chem. B.* **105**, 12857 (2001).
15. C. J. Coombes, *J. Phys. F: Metal Phys.* **2**, 441 (1972).
16. V. P. Skripov, V. P. Koverda, V. N. Skokov, *Phys. Status Solidi A.* **66**, 109 (1981).
17. J. F. Focza, A. Barna, P. B. Barna, *J. Vac. Sci. Technol.* **6**, 472 (1969).
18. M. Zhang at al., M. Y. Efremov, *Phys. Rev B.* **62**, 10548 (2000).

19. G. L. Allen, R. A. Bayles, W. W. Giles, W. A. Hesser, *Thin Solid Films*. **144**, 297 (1986).
20. G. Krausch, T. Detzel, *Appl. Phys. A: Mater. Sci. Process.* **53**, 324 (1991).
21. Q. Gulseren, F. Ercolessi, E. Tosatti, *Phys. Rev. B*. **51**, 7377 (1995).
22. M. Wautelet, *Phys. Lett. A*. **246**, 341(1998).
23. S. Prakash, T. Chakrabarty, A.K. Singh Prakash, *Biosensors and Bioelectronics*. **41**, 43(2013).
24. E. Kadir, B. Melda, T. Demet, N. Cengiz and A. A. Dursun, *Journal of Molecular Structure*. **1200**, 127060 (2020).
25. L. Kui, J. Zhao, G. Junjie, X. Changpeng and Wei, *J. Mater. Chem.* **5**, 19857(2017).
26. E. Mohamed, F. Philippe, D. Claude Le, M. G. Camelia and M. B. Jean, *RSC Advances*. **10**, 60 (2020).
27. J. Zhong, L.H. Zhang, Z.H. Jin, M.L. Sui, K. Lu, *Acta Materialia*. **49**, 2897(2001).
28. H. Saka, Y. Nishikawa, T. Imura, *Philosophical Magazine A: Physics of Condensed Matter, Structure, Defects and Mechanical Properties*. **57**, 895(1988).
29. K. Chattopadhyay, R. Goswami, *Progress in Materials Science*. **42**, 287.(1997).
30. H.W. Sheng, G. Ren, L.M. Peng, Z.Q. Hu, K. Lu, *Philosophical Magazine Letters*. **73**, 179(1996).
31. L. Grabaek, J. Bohr, E. Johnson, A. Johansen, L. Sarholt, Kristensen, H.H. Andersen, *Physical Review Letters*. **64**, 934(1990).
32. R. Narayanan, M. A. El-Sayed, *Nano Lett.* **4**, 1343 (2004).
33. Y. Li, J. Petroski, M. A. El-Sayed, *J. Phys. Chem. B*. **104**,10956 (2000).
34. M. S. Chen, D. W. Goodman, *Catal Today*. **111**, 22 (2006).
35. G. Guisbiers, G. Abudukelimu and D. Hourlier, *Nanoscale Research Letters*. **6**, 396 (2011).
36. G. Guisbiers, G. Abudukelimu, *J Nanopart Res* **15**, 1431 (2013).